Sensors & Diagnostics

PAPER

View Article Online
View Journal

Cite this: DOI: 10.1039/d5sd00134j

Electrochemical sensor for the detection of sunset yellow in food using a polyaniline/carbon nanopowder nanocomposite modified electrode

Judith Letsoalo, [ab] Gloria E. Uwaya[c] and Omolola E. Fayemi *[ab]

Received 18th July 2025,
Accepted 21st November 2025

DOI: 10.1039/d5sd00134j

rsc.li/sensors

Food items frequently face the risk of adulteration, which can lead to serious health consequences. An example of food fraud is the addition of synthetic azo dye sunset yellow (SY), for colouring food (SY-FCF). This study reports the design of an electrochemical sensor for the direct detection of SY at a glassy carbon electrode modified with a polyaniline (PANI) and carbon nanopowder (CNP) nanocomposite (GCE–PANI/CNP). The individual components of the sensor and the nanocomposite were characterised using FT-IR, UV-visible spectroscopy, XRD, SEM, and TEM. The developed electrochemical sensor (GCE/PANI/CNP) demonstrated optimal detection for SY using cyclic voltammetry and electrochemical impedance spectroscopy at approximately 0.8 V, compared to individual modified electrodes. The detection limit (LOD) was calculated to be 1.81 nM, with a broad linear detection range spanning from 1 to 194 nM, using square wave voltammetry. From the results obtained, it is concluded that the designed sensor can be a great tool for detecting sunset yellow in food samples.

1. Introduction

Consumers often base their food selection on a product's colour, which gives them a first impression of its flavour, texture, and freshness.[1] Consequently, it has become the justification for the addition of additives to food items.[1,2] Food adulteration, also known as food fraud, is in two primary forms: intentional acts carried out by dishonest producers, retailers, and processors seeking to make an economic profit, increase the weight and volume, improve the appearance, colour and flavor,[3] and extend the food's shelf life, and incidental occurrences that may occur during production, handling, storage, and other processes. Both intentional and unintentional adulteration may reduce the safety and the quality of food products, posing health risks to consumers.[3,4] Severe health effects such as chronic liver diseases, cancer, peptic ulcer diseases, kidney failure, electrolyte imbalance, bone marrow abnormalities, blood disorders, heart diseases, and skin problems can result from the use of food adulterants.[5,6] An example of food fraud is the addition of synthetic azo-dye sunset yellow for colouring food (SY-FC) with E number E110. Sunset yellow consists of two sulfonate groups located at either end of the molecule,[7] with two central aryl groups linked by an azo bridge (N═N).[7] The World Health Organization (WHO)[8] and the Food and Agriculture Organization (FAO)[8] have determined the acceptable daily intake (ADI)[8] for sunset yellow to be 4 mg per kilogram of body weight per day.[9] The maximum permitted levels of SY in non-alcoholic/alcoholic drinks are 50/200 mg L^{-1}.[10] When SY is consumed beyond the allowable daily intake, it can cause asthma, migraines, eczema, and other illnesses.[11,12]

Recently, numerous analytical methods have been developed in response to concerns about the sensitivity of reactions involving SY. These methods include thin-layer chromatography (TLC),[13] spectrophotometry,[1] high-performance liquid chromatography (HPLC),[14,15] mass spectrometry,[1] capillary electrophoresis, and electrochemical sensing.[1,10,16,17] Among these, HPLC is commonly employed due to its speed, selectivity, and reliability in producing accurate results. The detection of synthetic dyes using HPLC is often combined with other techniques, such as diode array detection,[1,18] UV-vis detection,[19] and mass spectrometric detection.[20] Although these techniques demonstrate commendable detection limits, none of these methodologies can lay claim to the combined advantages of cost efficiency, portability, rapidity, and facile manipulation inherent to electrochemical techniques.[21]

[a] Department of Chemistry, School of Physical and Chemical Sciences, Faculty of Natural and Agricultural Sciences, North-West University (Mafikeng Campus), Private Bag X2046, Mmabatho, 2735, South Africa.
E-mail: Omolola.Fayemi@nwu.ac.za
[b] Material Science Innovation and Modelling (MaSIM) Research Focus Area, Faculty of Natural and Agricultural Sciences, North-West University (Mafikeng Campus), Private Bag X2046, Mmabatho, 2735, South Africa
[c] Department of Chemistry, Durban University of Technology, Durban, South Africa

To enhance the performance of electrochemical techniques, nanomaterials are employed in designing electrochemical sensors.

Recently, carbon-based nanomaterials, including carbon nanopowder (CNP), have captivated significant attention due to their outstanding mechanical properties, high surface area, non-toxicity, and biocompatibility, opening numerous possibilities in the field of electrochemical devices, particularly electrochemical sensors and biosensors for detecting and quantifying various analytes. The unique electronic behaviour of these nanoparticles, which is dependent on their conducting–semiconducting structure, makes them highly suitable for these applications. Furthermore, their synthesis can be achieved through simple and low-cost procedures that are environmentally friendly.[22–24] PANI generates the most attraction among other conducting polymers due to the simplicity of synthesis, low cost, higher theoretical conductivity, wider range of the working potential window, and better stability.[25] Consequently, PANI has been used in the field of electrochemical sensors.[25] Carbon based nanomaterials can be applied individually or combined with other materials as a composite. The integration of carbon materials and conducting polymers such as PANI in the development of electrochemical sensors is highly favoured due to its exceptional performance, leveraging the unique benefits of each constituent.[25] For example, S. Jackson *et al.* (2025), developed a sensor using a GCE modified with PANI and carbon dots for alcohol detection with a low detection limit of 0.325 μM.[26] Also, the literature reports the use of a carbon nanotube (CNT) and PANI composite for electrochemical sensing of L-ascorbic acid and ammonia gas.[2,27] The literature search shows no report on the application of a CNP/PANI composite based electrochemical sensor for sunset yellow detection.

In this work, a carbon nanopowder (also known as carbon black) and polyaniline composite (PANI/CNP) is being explored in the development of an electrochemical sensor for the detection of SY.

2. Procedures and materials

2.1 Apparatus and chemicals

All reagents used in this study were of analytical grade. Sunset yellow (E110) with a dye content of 97%, *N*,*N*-dimethylformamide (99.8%), hydrogen chloride (HCl; 32%), aniline ($C_6H_5NH_2$), ammonium persulfate ($(NH_4)_2S_2O_8$, AP), and potassium hexacyanoferrate(III) ($K_3Fe(CN)_6$) were procured from Merck Chemicals, South Africa. Sodium phosphate dibasic (NaH_2PO_4) and monobasic (Na_2HPO_4) were procured from Merck, South Africa. A glassy carbon electrode (GCE) with a 3 mm diameter, a reference electrode containing Ag/AgCl saturated with KCl, and a platinum disk counter electrode were supplied by CH Instrument Inc. Carbon nanopowder (CNP) was commercially obtained from Aldrich Chemicals.

2.2 Synthesis of PANI

Polyaniline was prepared following an established method in the literature.[28,29] Approximately 0.312 g of aniline mass was added into a 1 M aqueous hydrochloric acid solution.[28] About 0.19 g of ammonium persulfate (APS) was dissolved in 10 mL of the same 1 M hydrochloric acid solution.[28,29] The two solutions were then combined together to achieve a 1 : 4 APS to aniline ratio[28] with a resulting PANI precipitate. The precipitate was collected through filtration, thoroughly washed with DI water, and subsequently dried in an oven at 65 °C for 24 h (Scheme 1).[28,29]

2.3 Preparation of the PANI/CNP nanocomposite

About 75 mg of the prepared PANI and 25 mg of the CNP were transferred into glass containers containing 3 mL DMF. The mixture was subjected to ultrasonication in a water bath at 25 °C for 48 h. The resulting paste was then used to modify the GCE using the drop-casting method.

2.4 Electrode pre-treatment

The bare GCE was cleaned by rubbing it in a spiral motion on a cleaning pad containing aqueous aluminium oxide, followed by an immediate rinse with distilled water. To remove any remaining organic impurities, the electrode was then immersed in ethanol and subsequently washed with distilled water under ultrasonication. After cleaning, the electrode was air-dried at room temperature.

2.5 Modification of the glassy carbon electrode

For electrode modification, the drop casting technique was employed. Specifically, approximately 10 μL of the nanomaterial and composite paste was deposited onto the surface of the clean bare GCE. The modified electrodes were subsequently heated in an oven at 50 °C for a duration of 3 min. The resulting modified electrodes were designated as GCE/PANI, GCE/CNP, and GCE/PANI/CNP.

2.6 Characterization of nanomaterials

Various spectroscopy techniques were employed for the characterization of electrode materials (PANI, CNP, and PANI/CNP).[28] The functional groups present in the materials were identified using Fourier transform infrared (FT-IR) spectroscopy,[30] their absorbance and wavelength properties were analysed using UV-visible (UV-vis) spectroscopy,[30] the

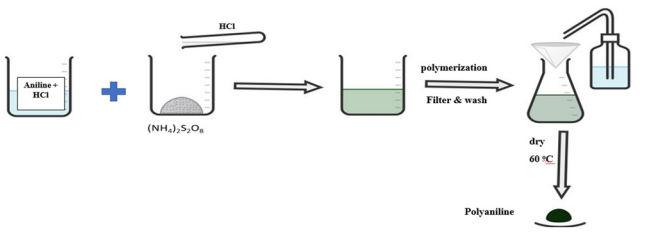

Scheme 1 Depiction of the synthesis method of PANI.

crystallinity of the nanomaterials was assessed on an X-ray diffractometer (XRD)[30] and energy-dispersive X-ray (EDS) spectroscopy provided information on their elemental composition. Moreover, microscopic characterization was carried out using transmission electron microscopy (TEM) and scanning electron microscopy (SEM),[31] with an emphasis on analysing their morphological and structural properties. Electrochemical analyses were performed on an Autolab potentiostat/galvanostat PGSAT-20 controlled by the software Nova 2.1.6, within a cell configured with a three-electrode[21] system, including the reference, working (PANI/CNP-modified GCE), and counter electrodes. The electrochemical characterization and analysis of the analyte were performed in a phosphate-buffered saline solution (10 mM PBS, pH 7), prepared using Na_2HPO_4 and NaH_2PO_4.

2.7 Sample preparation

In this study, Skopas snacks purchased from a local supermarket were used as a real sample. 10 g of the crushed Skopas snack was transferred to a beaker containing 200 mL of PBS at pH 7, then stirred for 15 min at room temperature. The mixture was subsequently filtered through Whatman filter paper, transferred to a vial, and stored in a refrigerator until analysis.

3. Results

3.1 FT-IR analysis

The spectrum of the nanoparticles, shown in Fig. 1, reveals a characteristic peak at 1610 cm^{-1} corresponding to C=C double bonds. The peak at 1783 cm^{-1} is attributed to the carboxylic group (C=O) stretching vibration of COOH attached to CNP groups. Additionally, the fingerprint region shows bands associated with an aromatic structure for CNP.[32,33] The PANI spectrum displays key peaks at 800 cm^{-1}, 1100 cm^{-1}, 1292 cm^{-1}, 1469 cm^{-1}, and 1540 cm^{-1}. The peaks at 1469 cm^{-1} and 1540 cm^{-1} are linked to the stretching vibrations of C=C bonds in the benzenoid and quinoid rings, respectively. The absorption bands observed at 1292 cm^{-1} and 1100 cm^{-1} are attributed to the stretching vibrations of C–N bonds in the secondary aromatic amine.[28,34] The 800 cm^{-1} vibrational band corresponds to the C–H out-of-plane bending mode in substituted aromatic compounds.[28,34–37] The PANI/CNP composite also shows the same characteristic peaks noticed in PANI, although with observable reduction in peak intensity. The decrease in peak intensity observed in the nanocomposite spectrum can indicate effective CNP integration into the polyaniline matrix.

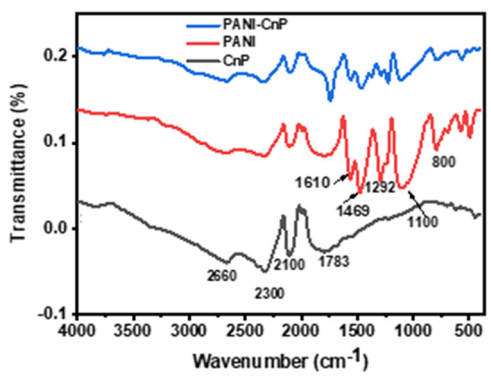

Fig. 1 FTIR spectra of CNP, PANI and the PANI/CNP nanocomposite.

3.2 Ultraviolet-visible spectroscopy

The optical properties of PANI, CNP, and PANI/CNP dissolved in DMF were evaluated across a wavelength range of 200 to 900 nm, as illustrated in Fig. 2. CNP exhibits a prominent absorption band with the highest vibrational intensity at 288 nm, attributed to the π–π* transition within the carbon material's structure.[38] The PANI spectrum displayed peaks at 620 nm and 325 nm, corresponding to the π–π* transition of benzene ring charge and the electron transfer between quinoid and benzenoid rings, respectively.[28,39] The shift observed in the peaks of the absorbance in the UV-vis spectrum of the nanomaterials and the PANI/CNP composite indicates the successful production of PANI/CNP nanocomposites and the existence of potential chemical interactions between the PANI and CNP nanoparticles. The interactions of the nanomaterials (CNP and PANI) can be seen in the nanocomposite with the appearance of a new peak which is absent in PANI. Additionally, the blue shift from 325 nm to 380 nm and the red shift from 620 nm to 530 nm, with reduction observed in the nanocomposite spectrum, suggest the interaction of the quinoid with the CNP.

3.3 XRD analysis

Fig. 3(a) presents the X-ray diffraction (XRD) pattern of polyaniline, showing four distinct peaks at 10.7°, 17.5°, 20.6°, and 25.5°, corresponding to the (001), (011), (020), and (200) planes, respectively. These sharp peaks indicate that the polymer is semi-crystalline, which is attributed to the presence of benzenoid and quinonoid groups in the polyaniline structure.[40,41] Additionally, a characteristic peak

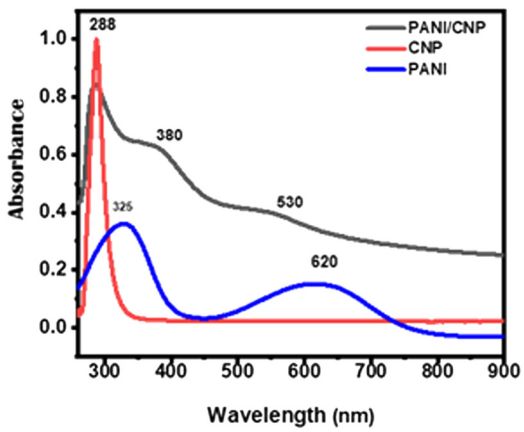

Fig. 2 UV-vis spectra of CNP, PANI and PANI/CNP.

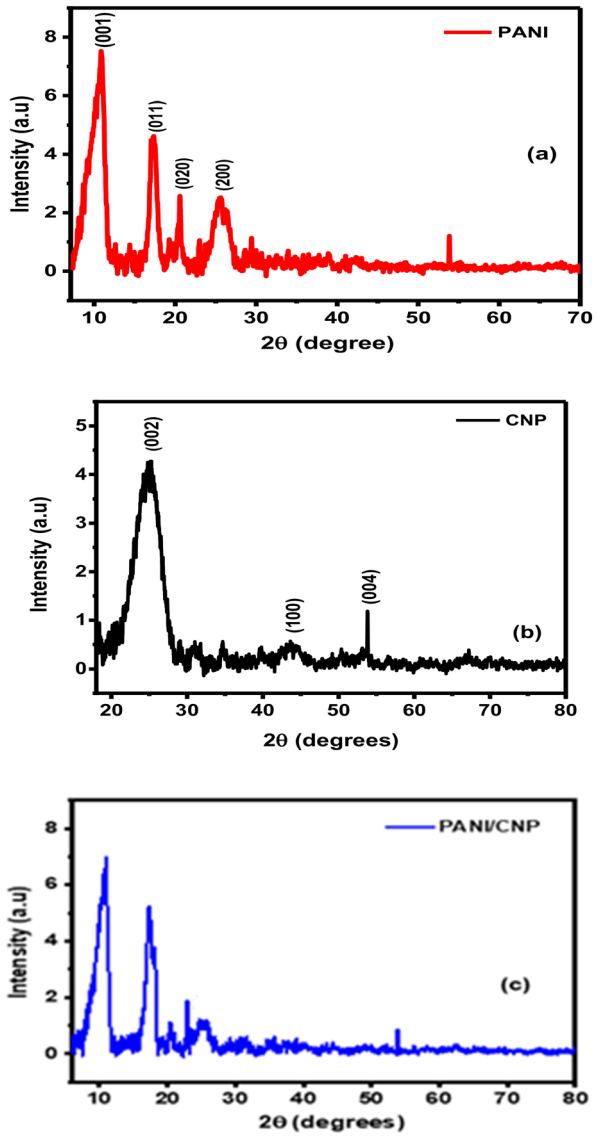

Fig. 3 XRD diffractograms of (a) PANI, (b) CNP and (c) PANI/CNP.

at 26.1° is observed in the CNP and the nanocomposite (Fig. 3c), corresponding to the (002) plane, which is typical of carbon materials. Low-intensity peaks, characteristic of well-graphitized multi-walled carbon materials, appear at 43.6° (100) and 54.0° (004), consistent with the values reported in the literature.[42,43]

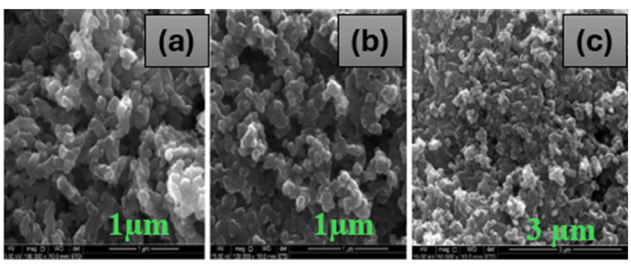

Fig. 4 SEM micrographs of (a) PANI, (b) CNP and (c) PANI/CNP.

3.4 Scanning electron microscopy analysis

To evaluate the shape and morphology of the nanoparticles, SEM analysis was performed. Fig. 4(a–c) presents the SEM micrographs of PANI, CNP and PANI/CNP, respectively.[44] In Fig. 4(b), the CNP micrograph reveals the agglomeration of spherical shaped particles with some voids. The same trend is noticed in the image of PANI, although less agglomerated spherical particles than CNP (Fig. 4(a)). The nanocomposite (PANI/CNP) morphology shows densely agglomerated spherical shaped particles with a noticeable reduction in the size of the particles and lesser voids in comparison to the CNP and PANI micrographs. The dense aggregation and decrease in particle size with minute voids suggest a strong interaction between PANI and CNP, and confirms that the PANI/CNP composite was successfully synthesized.

3.5 Energy dispersive X-ray spectroscopy

The EDS spectra for PANI, CNP, and PANI/CNP are presented in Fig. 5(a–c). The detection of nitrogen (N = 10.28%) and carbon (C = 67.4%) peaks verifies the successful synthesis of PANI molecules and the formation of the PANI/CNP nanocomposite. The presence of copper (Cu) and chlorine (Cl) in CNP and PANI, respectively, could probably have resulted from the instrument sample holder. Meanwhile, the existence of sulfur (S) in PANI and PANI/CNP could be residual sulfur from ammonium persulfate used in the PANI synthesis. The observable differences in weight (%) of C, N, and O in the nanomaterials indicate possible interactions between CNP and PANI.

3.6 Transmission electron microscopy

TEM is an important tool in scientific study, particularly for determining the magnitude of produced nanomaterials.[28] Fig. 6a–c shows the TEM images of PANI, CNP and PANI/CNP accordingly, at a magnification of 200 nm. The TEM micrograph of PANI (Fig. 6a) shows a unique short-rod shape with spherical dark spots of PANI, agglomerated in certain points, likely as a result of π–π interactions between the PANI molecules.[29] Such observations are made on the SEM micrograph of PANI as well.[40] The TEM picture of CNP (Fig. 6b) shows that the carbon nanopowder has a pseudo-spherical structure with smaller dark spots. The darker spots in the micrograph indicate CNP aggregation, which results in two different aggregate types. The nanocomposite TEM image reveals the attachment of CNP on PANI (Fig. 6(c)), suggesting successful synthesis of PANI/CNP.

3.7 Electrochemical characterization

Electrochemical characteristics of the modified electrodes were assessed using cyclic voltammetry (CV) in a 10 mM redox probe ($[Fe(CN)_6]^{3-/4-}$) prepared in 0.1 M phosphate-buffered saline at pH 7 and a temperature of 25 °C (ref. 21) at 25 mV s^{-1}. The oxidation current responses for the bare GCE, GCE/CNP, GCE/PANI, and GCE/PANI/CNP are 3.888,

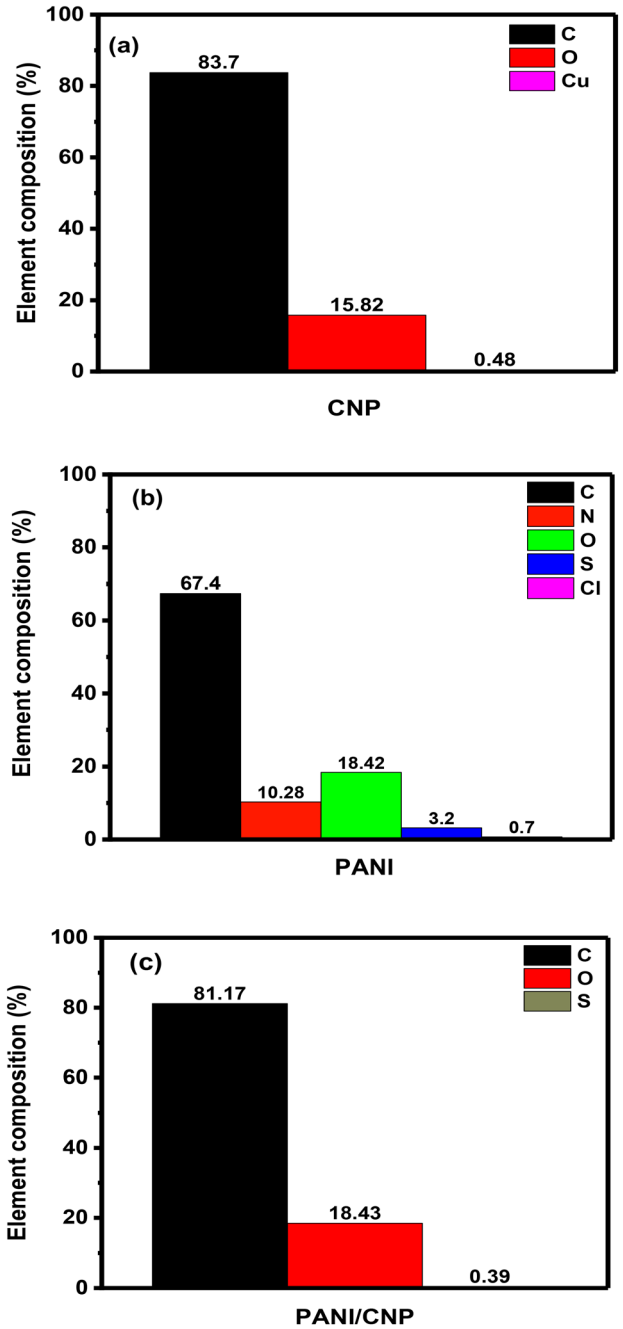

Fig. 5 EDS spectra showing the elemental composition of (a) CNP, (b) PANI and (c) PANI/CNP.

53.464, 29.242, and 47.691 μA, respectively, as illustrated in Fig. 7. From the results, PANI/CNP demonstrated optimal current response, suggesting excellent electrical conductivity and surface properties, facilitating efficient transfer of electrons between the modified electrode and the redox probe. The bare GCE exhibited the lowest current response, in contrast to GCE/CNP and GCE/PANI, demonstrating that these materials significantly improve electron transfer kinetics compared to the unmodified electrode.

$$I_p = 2.69 \times 10^5 n^{3/2} A D^{1/2} C v^{1/2} \quad (1)$$

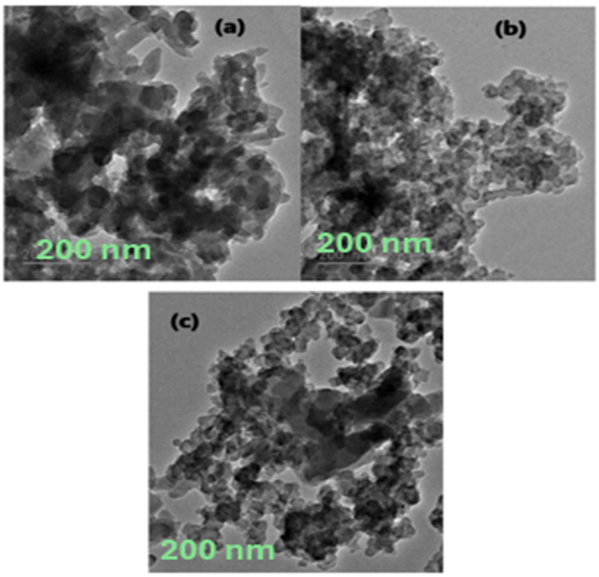

Fig. 6 TEM images of (a) PANI, (b) CNP, and (c) PANI/CNP.

According to the Randles–Sevcik equation[21] (1), I_p, v, n, A, C and D correspond to the peak current (A), scan rate (V s^{-1}),

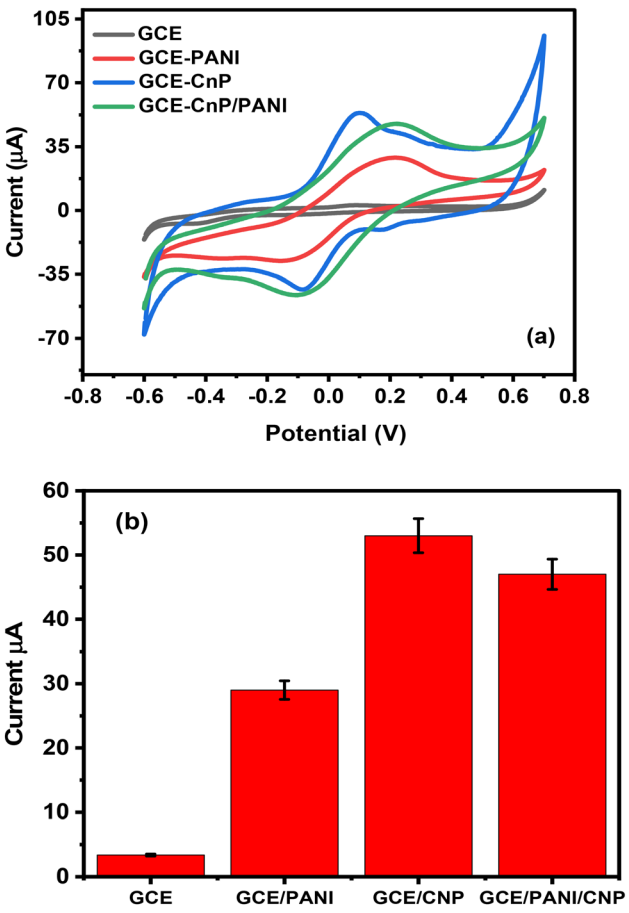

Fig. 7 (a) Cyclic voltammograms of electrodes and (b) their current response in 10 mM $[Fe(CN)_6]^{3-/4-}$ at a scan rate of 25 mV s^{-1}.

number of electrons transferred, electrode surface area (cm^2), concentration (mol cm^{-3}), and diffusion coefficient (cm^2 s^{-1}), respectively.[21] The surface areas (A) of the bare GCE, GCE/CNP, GCE/PANI, and GCE/PANI/CNP were calculated to be 0.005, 0.072, 0.039, and 0.064 cm^2, respectively. The modified electrode exhibited the highest current response and the largest surface area, suggesting that the modification significantly improved the electrode's surface area and potentially its conductivity. Table 1 summarises the parameters obtained from CV measurements for all four electrodes (GCE, GCE/CNP, GCE/PANI, and GCE/PANI/CNP). The anodic to cathodic peak current ratio for all the electrodes is approximately 1, suggesting a reversible electrochemical process. This enhanced electronic conductivity promotes more effective electron transfer between the modified electrode and the redox probe.

Electrochemical impedance spectroscopy (EIS) was employed to further understand the charge resistivity of the electrodes in a 10 mM $[Fe(CN)_6]^{3-/4-}$ solution. The Nyquist plots for GCE, GCE/CNP, GCE/PANI, and GCE/PANI/CNP recorded in a 10 mM $[Fe(CN)_6]^{3-/4-}$ solution are presented in Fig. 8(a). Additionally, Fig. 8(b) illustrates the analogous circuits used to fit the EIS data for these electrodes (GCE/CNP, GCE/PANI, and GCE–PANI/CNP). The numerical values of the fitted parameters, including solution resistance (R_s), charge transfer resistance (R_{ct}), the exponent of the constant phase element (N), and the Warburg impedance (W), are listed in Table 2. The errors associated with these parameters, as calculated from the EIS data fitting, are provided in parentheses in Table 2.

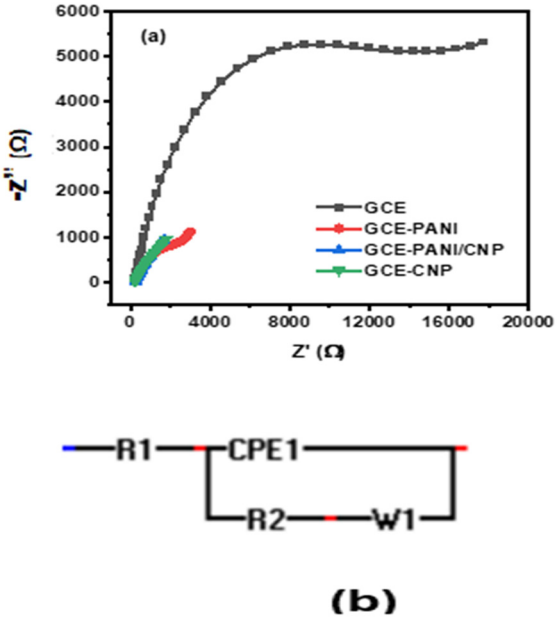

Fig. 8 EIS spectra (Nyquist plot) of (a) bare GCE and modified GCE/CNP, GCE/PANI and GCE/PANI/CNP in 10 mM $[Fe(CN)_6]^{3-/4-}$ (pH 7); (b) equivalent electrochemical circuit of the EIS data in (a).

3.8 Electrocatalytic response of PANI/CNP to SY oxidation

The electrochemical behaviour of SY on the bare GCE and the modified electrodes was assessed through CV at a sweep rate of 25 mV s^{-1} in 0.1 mM SY solution prepared in 10 mM PBS (pH 7). The voltammetric responses of the electrodes as shown in Fig. 9(a) demonstrate a reversible electrochemical process with well-defined redox peaks. All cyclic voltammograms exhibited two key peaks: an anodic peak corresponding to SY oxidation at a potential range of 0.29–0.34 V and a cathodic peak occurring between 0.09 and 0.125 V. The oxidation peak currents (I_{pa}) with the associated potentials in parentheses for SY at the bare GCE, GCE/CNP, GCE/PANI, and GCE/PANI/CNP were recorded as 26.995 μA (0.347 V), 235 μA (0.292 V), 192.529 μA (0.294 V), and 294 μA (0.294 V), respectively. Fig. 9(b) presents a bar graph of the current responses for the bare and modified electrodes. The oxidation peak current at the GCE/PANI/CNP electrode was approximately ten times higher than that of the unmodified GCE, suggesting that the combination of CNP and PANI provided a synergistic effect that significantly enhanced the electrocatalytic activity of the composite for SY oxidation. Overall, the electrodes' current responses followed the trend: GCE/PANI/CNP > GCE/CNP > GCE/PANI > GCE, as shown in Fig. 9(b).

3.9 Influence of pH on SY oxidation

The influence of pH on the SY oxidation peak current and potential was evaluated in 0.1 mM PBS with varying pH ranges of 3–9, employing CV at a 25 mV s^{-1} scan rate. Fig. 10 shows the maximum oxidation current response for SY at pH 7, suggesting that pH 7 is the best for determining the sensitivity of SY. Consequently, pH 7 was used in this study. Also, as the pH increase, the oxidation peak potential shifted

Table 1 The comparative parameters from the cyclic voltammograms of the unmodified and modified electrodes obtained in the 10 mM $[Fe(CN)_6]^{3-/4-}$ redox couple in PBS (pH 7) at a scan rate of 25 mV s^{-1}

Electrodes	I_{pa} (μA)	E_{pa} (V)	I_{pc} (μA)	E_{pc} (V)	ΔE_p (V)	$\frac{I_{pa}}{I_{pc}}$	A (cm^2)
GCE	30.888	0.0817	−3.0730	0.2083	0.29	1.27	0.005
GCE–CNP	53.464	0.1076	−43.4239	0.0857	0.19	1.23	0.072
GCE–PANI	29.242	0.2192	−26.6723	0.1266	0.35	1.10	0.039
GCE–PANI/CNP	47.691	0.2303	−46.3101	0.1043	0.33	1.03	0.064

Table 2 EIS parameters of the bare GCE and modified electrodes with errors in parentheses

Electrode	R_s (kΩ)	R_{ct} (kΩ)	CPE (μF)	W (F)/*C (μF)	N	X^2
GCE	0.19 (3.68)	16.44 (5.77)	19.4 (3.27)	7491 (10.0)	0.86 (0.63)	0.0
GCE–CNP	5.4×10^{-14} (2.38)	6.10 (8.30)	7.35 (4.50)	1434 (9.36)	0.94 (0.62)	0.0007
GCE–PANI	0.18 (0.34)	3.2 (0.56)	8.41 (2.51)	752.5 (7.46)	0.95 (0.35)	0.0
GCE–PANI/CNP	0.16 (0.12)	1.36 (0.24)	21.6 (3.13)	797.4 (9.9)	0.87 (0.54)	$1.77 \times 10^{-0.5}$

progressively towards the negative potentials, indicating the participation of protons in the oxidation process of SY.[2,45,46]

3.10 Influence of the scan rate on the oxidation of SY at GCE–PANI/CNP

The influence of the scan rate on the oxidation of SY was examined at different scan rates from 5–850 mV s^{-1} in PBS at pH 7. Fig. 11(a) shows a progressive increase in the oxidation peak current with rising scan rates. Additionally, the voltammograms demonstrated a rightward shift in potential with each increment in the scan rate. The linear correlations between the square root of the scan rate ($v^{1/2}$) and peak currents (I_{pa} and I_{pc}) were described by the equations:

$$I_{pa}\ (\mu A) = 10.876x - 50.787v^{1/2}(v)^{1/2}\ (R^2 = 0.9905) \text{ and}$$

$$I_{pc}\ (\mu A) = -1.7654x - 5.13v^{1/2}(v)^{1/2}\ (R^2 = 0.9373).$$

These results indicate the occurrence of both diffusion-controlled and surface-confined processes at the electrode.[21] The number of electrons transferred (n) and the electron transfer coefficient (α) determined from the relationship between the anodic peak potential (E_{pa}) and the natural log v, in accordance with Laviron's eqn (2) and (3),[47,48] were found to be 2 and 0.63, respectively. The corresponding reaction mechanism of SY at the modified PANI/CNP electrode is presented in Scheme 2.

$$E_{pa} = \frac{E^\circ + 2.303RT}{(1-\alpha)nF \log v} \quad (2)$$

$$E_{pc} = \frac{E^\circ - 2.303RT}{\alpha nF \log v} \quad (3)$$

The correlation between the log v and peak potentials is essential for elucidating the kinetics and mechanisms underlying electrochemical processes on electrodes. Linear plots of log v against the peak potentials, such as those described in Fig. 11, typically indicate that the electrochemical process is controlled by a kinetic mechanism. The Tafel value for the PANI/CNP

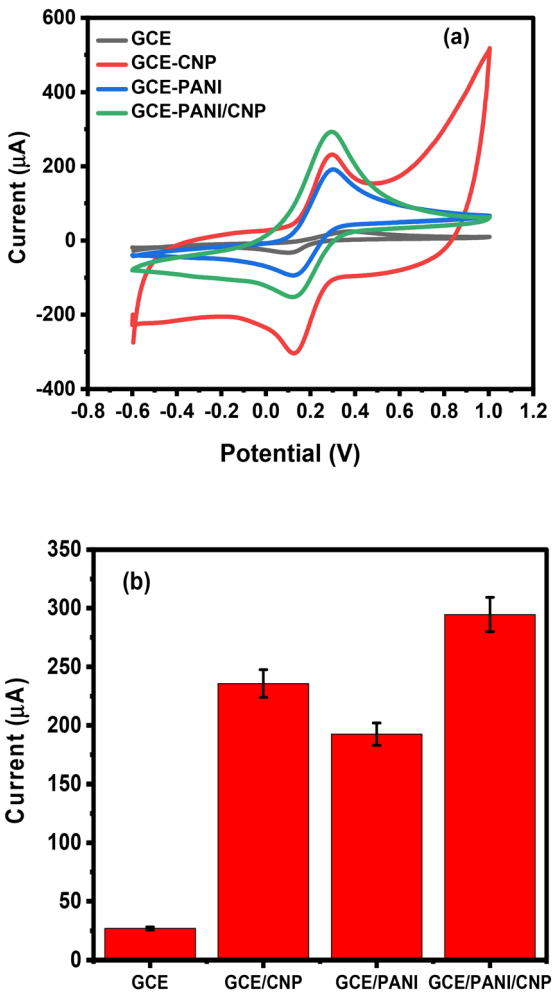

Fig. 9 (a) CVs and (b) bar graph of the oxidation peak current response for 0.1 mM SY at the unmodified and modified electrodes recorded at a 25 mV s^{-1} scan rate.

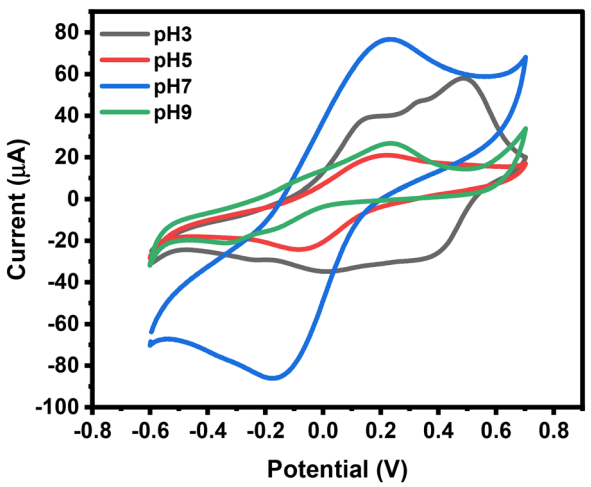

Fig. 10 Cyclic voltammograms of 0.1 mM SY at different pH values.

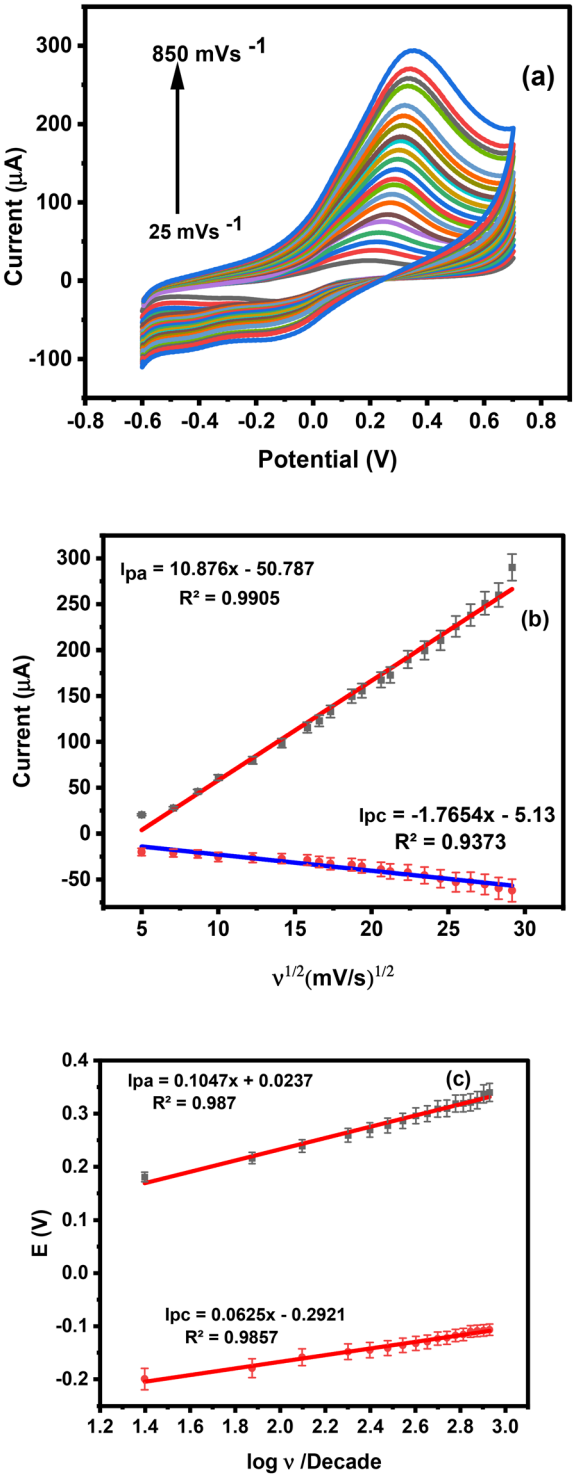

Fig. 11 (a) Cyclic voltammetric response of the PANI/CNP electrode in 0.1 mM SY in PBS, pH 7, at varying scan rates of 25 to 850 mV s^{-1}, (b) plots of *I* (μA) *vs.* $\nu^{1/2}$, and (c) plots of *E* (V) *versus* log *v*.

nanocomposite modified electrode was determined based on the slope of the plot E_p against log ν (the linear equations presented in eqn (4) and (5) from Fig. 11(c)) using eqn (6)[28] was found to be 0.052.V dec^{-1} and 0.0313 V dec^{-1} for E_{pa} and E_{pc}, respectively. The Tafel values (b) are less than the

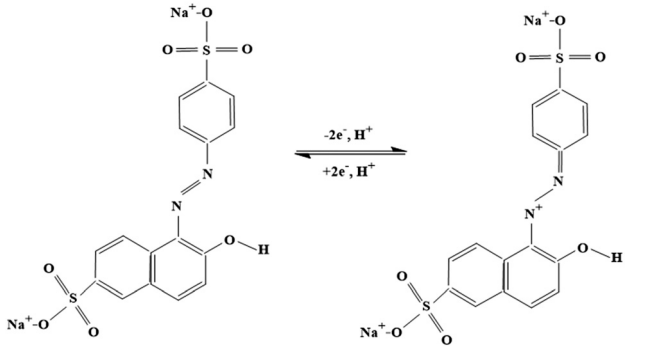

Scheme 2 Proposed mechanism of SY.

theoretical value (0.118 V dec^{-1}) for a one-electron process, suggesting non-occurrence of adsorption on the modified electrode's surface.[28]

$$E_{pa} = 0.1047x + 0.023 \ (R^2 = 0.987) \quad (4)$$

$$E_{pc} = 0.0625x - 0.2921 \ (R^2 = 0.9857) \quad (5)$$

$$E_p = \left(\frac{b}{2}\right) \log \nu + \text{constant} \quad (6)$$

3.11 Electroanalysis of SY at the PANI/CNP modified GC electrode

The influence of varying concentrations on the current response of SY was determined using SWV under 0.01 V potential step, 0.001 V amplitude, a deposition time of 10 seconds, and a frequency of 25 Hz. The oxidation peak current (I_{pa}) increased with increasing concentration of SY over a dynamic linear range of 1–194 nM as shown in Fig. 12(a), showing the dependence of the peak current of SY with the increase in the SY concentration. The linear relationship for SY concentrations and I_{pa} is presented in Fig. 12(b) in PBS with a pH of 7 with the linear regression equation of *I* (μA) = 9.1159 × 10^8 + 30.025 [SY] and a 0.9909 correlation coefficient. The limits of detection and quantification (LOD and LOQ) were computed to be 1.81 nM and 5.49 nM employing eqn (7) and (8), respectively, where SD represents the standard deviation of the peak current, over a slope of the calibrated plot. This LOD is favorably comparable with some SY sensors reported in studies (see Table 4).

$$\text{LOD} = \frac{3.3 \times \text{SD}}{\text{Slope}} \quad (7)$$

$$\text{LOQ} = \frac{10 \times \text{SD}}{\text{Slope}} \quad (8)$$

3.12 Real sample analysis

To check the practical rationality of the designed electrode, SY was determined in a real sample (Skopas snacks) following a well-established procedure (standard addition)

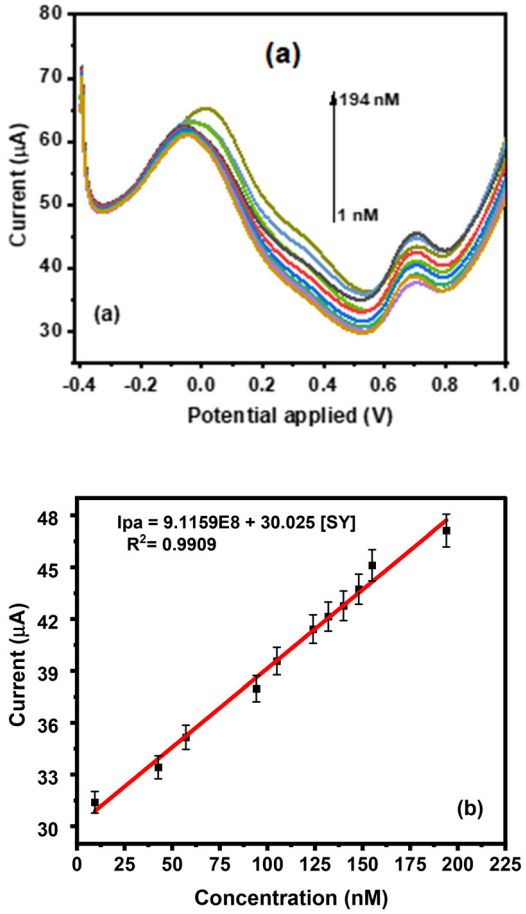

Fig. 12 (a) Square wave voltammograms at different SY concentrations (1–194 nM) in PBS at pH 7. (b) The corresponding calibration plot depicting the relationship between of I_p (μA) and SY concentrations.

using SWV. The SWV results of unspiked and spiked samples were obtained under optimal conditions: a deposition time of 10 seconds, a potential step of 0.01 V, a frequency of 25 Hz, and an amplitude of 0.001 V.[54] Table 3 shows the result obtained for real SY sample analysis with recovery values between 95 and 99% with an average RSD (%) value of 2.139 (n = 3). The good recoveries confirm that the detection of SY at the modified GCE–PANI/CNP electrode is reliable for the direct determination of SY in food samples.

3.13 Interference studies

Since SY is an anionic dye commonly found in food alongside other anionic and cationic dyes, the selectivity of GCE–PANI/CNP sensor electrodes was examined in the presence of methylene blue (MB), a cationic dye. This assessment was conducted using square wave voltammetry (SWV). Fig. 13(a) shows the square wave voltammogram of 0.01 mM of MB used against 0.1 mM SY with the MB peak appearing around −0.2 V and that of SY at around 0.7 V.[55,56] Fig. 13(b) shows that the electrode exhibited strong selectivity with a constant methylene blue concentration of 0.01 mM. The electrode was able to detect SY as the concentrations increased from 14.7 μM to 32 μM in the presence of MB (Table 5).

3.14 Stability studies

The stability and reproducibility of the GCE–PANI/CNP-modified electrode were evaluated using cyclic voltammetry over twenty-five consecutive scans at a 25 mV s^{-1} sweep rate in a 10 mM $K_3[Fe(CN)_6]$ solution prepared in 10 mM PBS (pH 7.0). A 29.8% increase in the oxidation peak current was observed with no observable shift of peak potential (Fig. 14). The increase in oxidation current could be potentially due to an increase in the electroactive surface area, allowing a greater interaction with the probe solution over time.

Table 3 Peak summary for the comparative voltammograms of the different electrodes in 0.1 mM SY in PBS at pH 7 and 25 mV s^{-1} scan rate

Electrodes	I_{pa} (μA)	E_{pa} (V)	I_{pc} (μA)	E_{pc} (V)	ΔE_p (V)	$\frac{I_{pa}}{I_{pc}}$	A (cm^2)
GCE	26.995	0.347	−29.881	0.094	0.253	0.903	0.036
GCE–CNP	235.823	0.292	−302.094	0.125	0.167	0.780	0.315
GCE–PANI	192.530	0.294	−98.642	0.117	0.177	1.952	0.257
GCE–PANI/CNP	294.397	0.294	−148.727	0.117	0.177	1.979	0.394

Table 4 Comparison with other chemically modified electrodes towards the detection of sunset yellow

Modified electrode	Technique	Linear range (μM)	LOD (μM)	Ref.
GO[a]/MWCNTs/GCE	LSV	0.09–30	0.025	49
MWNT film-modified GCE	DPV	0.0553–11.05	0.0244	50
Au[b]/RGO[c]/GCE	DPV	0.002–109.14	0.002	51
Chitosan/graphene/GCE	CV	0.2–100	0.0666	52
GN[d]/TiO_2[e]-CPE	SWV	0.02–2.05	0.006	53
rGO-g-CN[f]/ZnO[g]-AuNPs[h]/GCE	SWV	0.005–0.085	0.0013	54
GCE/CNP/PANI	SWV	0.001–0.194	0.00181	This work

[a] Graphene oxide. [b] Gold. [c] Reduced graphene oxide. [d] Graphene. [e] Titanium dioxide. [f] Graphitic carbon nitride. [g] Zinc oxide. [h] Gold nanoparticles.

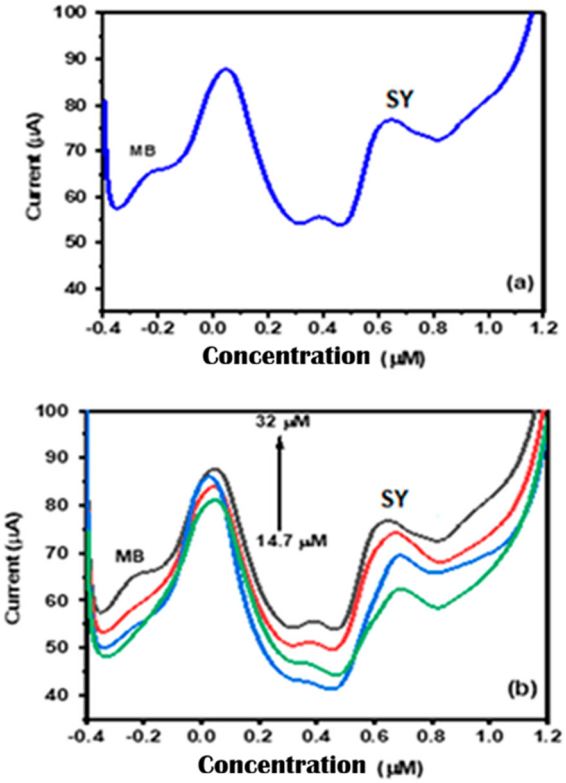

Fig. 13 (a) Square wave voltammogram displaying the characteristic peaks of methylene blue (MB) and SSY. (b) SWV voltammograms recorded while maintaining a constant MB concentration of 0.1 mM, with a gradual increase in SY concentration from 14.7 to 32 μM on the GCE–PANI/CNP-modified electrode.

Table 5 Recovery studies of sunset yellow (SY) at GCE–PANI/CNP

Sample (Skopas snacks)	Amount added (μM)	Amount found (μM)	% Recovery	RSD (% n = 3)
1	9.09	8.52	95	2.139
2	9.09	8.80	98	2.139
3	9.09	8.87	99	2.139

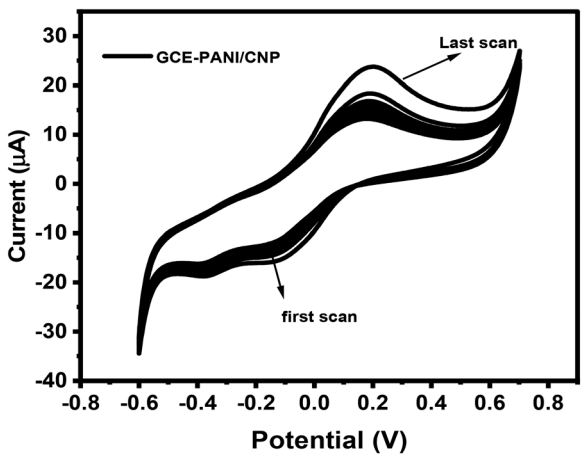

Fig. 14 The stability of the GCE–PANI/CNP modified electrode in 0.1 mM SY prepared in 10 mM PBS, pH 7, at a 25 mV s^{-1} scan rate.

4. Conclusions

The addition of adulterants, such as sunset yellow, in food has serious health effects on consumers; hence, there is a need to develop a sensor to detect the concentrations of such adulterants in food. PANI functionalized with CNP to form nanocomposites was used in detecting sunset yellow (SY) in a food sample. To confirm the correct synthesis of this material, various characterization techniques, including morphological, spectroscopic, microscopic, and structural analyses, were employed. Electrochemical experiments were performed using SWV, CV and EIS, demonstrating that the GCE–PANI/CNP nanocomposite-modified electrodes exhibit enhanced electron transport and a superior response to SY detection compared to other tested electrodes. The SY detection process at the GCE–PANI/CNP nanocomposite-modified electrode was found to be diffusion-controlled. The sensor provides a low LOD of 1.8 nM and a broad linear range from 1 to 194 nM, indicating its improved sensitivity over previously fabricated sensors.

Additionally, when tested against MB, the sensor could reliably distinguish SY from MB, showing good selectivity. Further validation of the sensor was conducted by testing it on real food samples. The sensor achieved high recovery rates when used to detect SY in Skopas snacks, highlighting its potential for application in the food industry. Despite moderate stability observed in comparing the first and last of the 25 scans in the PANI/CNP nanocomposite voltammogram, other favourable performance metrics suggest that this sensor is a strong candidate for commercialisation. It shows promise for point-of-care SSY detection in food products and other real samples at nanomolar levels, supporting consumer safety and regulatory compliance.

Author contributions

OEF: conceptualization, supervision, reviewing, and editing. JL: synthesis and electrochemical investigations, data curation, interpretation of data, and manuscript writing. All authors OEF, JL and GEU reviewed the manuscript.

Conflicts of interest

There are no conflicts to declare.

Data availability

Data used in this study will be made available upon request from the corresponding author.

Acknowledgements

The authors acknowledge the National Foundation Research (NRF), the North-West University and MaSim.

References

1 K. Rovina, L. A. Acung, S. Siddiquee, J. H. Akanda and S. M. Shaarani, *Food Anal. Methods*, 2017, **10**, 773–787.
2 F. S. Lisboa, E. G. C. Neiva, M. F. Bergamini, L. H. Marcolino Junior and A. J. G. Zarbin, *J. Braz. Chem. Soc.*, 2020, **31**, 1093–1100.
3 G. Kaur, R. Bhari and K. Kumar, *Crit. Rev. Biotechnol.*, 2024, **44**, 547–561.
4 M. Momtaz, S. Y. Bubli and M. S. Khan, *Foods*, 2023, **12**, 199.
5 D. Yeasmin, M. Baker, A. H. M. Kamal, M. S. Islam, M. Rahman, P. J. Winch and L. Unicomb, *BMC Public Health*, 2022, **23**, 206.
6 N. Raturi, J. Aman and C. Sharma, *Octa J. Biosci.*, 2022, **10**, 37–50.
7 N. Kizil, E. Basaran, D. Erbilgin, M. L. Yola, F. Uzcan and M. Soylak, *Microchem. J.*, 2022, **181**, 107734.
8 K. Rovina, S. Siddiquee and S. M. Shaarani, *Trends Food Sci. Technol.*, 2017, **65**, 68–79.
9 L. C. A. Feitosa, P. D. S. Rodrigues, A. S. Da Silva, A. D. O. Rios and F. Cladera-Olivera, *Food Addit. Contam.,: Part A*, 2017, **34**, 687–694.
10 K. Rovina, P. P. Prabakaran, S. Siddiquee and S. Md. Shaarani, *TrAC, Trends Anal. Chem.*, 2016, **85**, 47–56.
11 M. N. N. Begam, K. Muthukumaran, P. Thamarai and J. P. Joshua, *Global NEST J.*, 2022, **24**, 276–285.
12 Y. Zheng, S. Mao, J. Zhu, L. Fu, N. Zare and F. Karimi, *Food Chem. Toxicol.*, 2022, **164**, 113019.
13 F. I. de Andrade, M. I. F. Guedes, Í. G. P. Vieira, F. N. P. Mendes, P. A. S. Rodrigues, C. S. C. Maia, M. M. M. Ávila and L. de Matos Ribeiro, *Food Chem.*, 2014, **157**, 193–198.
14 S. Bonan, G. Fedrizzi, S. Menotta and C. J. D. Elisabetta, *Dyes Pigm.*, 2013, **99**, 36–40.
15 M. A. Prado, L. F. Vilas Boas, M. R. Bronze and H. T. Godoy, *J. Chromatogr. A*, 2006, **1136**, 231–236.
16 K. Yamjala, M. S. Nainar and N. R. Ramisetti, *Food Chem.*, 2016, **192**, 813–824.
17 K. Hroboňová, J. Lehotay, J. Čižmárik and J. Sádecká, *J. Liq. Chromatogr. Relat. Technol.*, 2013, **36**, 486–503.
18 P. Qi, Z.-h. Lin, G.-y. Chen, J. Xiao, Z.-a. Liang, L.-n. Luo, J. Zhou and X.-w. Zhang, *Food Chem. Mass Spectrom.*, 2015, **181**, 101–110.
19 Y. P. Zhang, Y. J. Zhang, W. J. Gong, A. I. Gopalan and K.-P. Lee, *J. Chromatogr. A*, 2005, **1098**, 183–187.
20 F. Gosetti, P. Frascarolo, E. Mazzucco, V. Gianotti, M. Bottaro and M. C. Gennaro, *J. Chromatogr. A*, 2008, **1202**, 58–63.
21 S. E. Elugoke, O. E. Fayemi, A. S. Adekunle, B. B. Mamba, T. T. Nkambule and E. E. J. F. Ebenso, *FatChem*, 2022, **33**, 100372.
22 M. Antunes and J. I. Velasco, *Prog. Polym. Sci.*, 2014, **39**, 486–509.
23 E. Asadian, M. Ghalkhani and S. Shahrokhian, *Sens. Actuators, B*, 2019, **293**, 183–209.
24 N. L. Teradal, R. D. Tandel and J. Seetharamappa, *Mater. Sci. Energy Technol.*, 2019, **2**, 337–344.
25 H. Wang, J. Lin and Z. X. Shena, *J. Sci.: Adv. Mater. Devices*, 2016, **1**, 225–255.
26 S. Jackson, M. Taylor, R. Kumar, A. K. Shringi, T. Leung and U. Riaz, *Nanomaterials*, 2025, **15**, 593.
27 G. Wu, H. Du, Y. L. Cha, D. Lee, W. Kim, F. Feyzbar-Khalkhali-Nejad, T. S. Oh, X. Zhang and D. J. Kim, *Sens. Actuators, B*, 2023, **375**, 132858.
28 O. E. Fayemi, J. Makgopa and E. Elugoke, *Mater. Res. Express*, 2024, **10**, 125603.
29 O. E. Fayemi, A. S. Adekunle, B. E. K. Swamy and E. E. Ebenso, *J. Electroanal. Chem.*, 2018, **818**, 236–249.
30 J. T. Mhlongo, *Master's thesis*, University of the Witwatersrand, 2023.
31 S. E. Elugoke, O. E. Fayemi, A. S. Adekunle, P.-S. Ganesh, S. Y. Kim and E. E. Ebenso, *J. Electroanal. Chem.*, 2023, **929**, 117120.
32 T. L. Ba, M. Bohus, I. E. Lukács, S. Wongwises, G. Gróf, K. Hernadi and I. M. Szilágyi, *Nanomaterials*, 2021, **11**, 608.
33 V. Țucureanu, A. Matei and A. M. Avram, *Crit. Rev. Anal. Chem.*, 2016, **46**, 502–520.
34 B. K. Sharma, A. K. Gupta, N. Khare, S. K. Dhawan and H. C. Gupta, *Synth. Met.*, 2009, **159**, 391–395.
35 M. Ibrahim and E. Koglin, *Acta Chim. Slov.*, 2005, **52**, 159–163.
36 X. Gu, Z. Chen, Y. Li, J. Wu, X. Wang, H. Huang, Y. Liu, B. Dong, M. Shao and Z. Kang, *ACS Appl. Mater. Interfaces*, 2021, **13**, 24814–24823.
37 T. S. Kuznetsova, A. E. Burakov, O. A. Ananyeva, I. V. Burakova, A. E. Memetova, V. O. Yarkin and A. G. Tkachev, *Colloid J.*, 2024, **86**, 408–417.
38 F. Mocci, L. de Villiers Engelbrecht, C. Olla, A. Cappai, M. F. Casula, C. Melis, L. Stagi, A. Laaksonen and C. M. Carbonaro, *Chem. Rev.*, 2022, **16**, 13709–13799.
39 A. Rahy and D. J. Yang, *Mater. Lett.*, 2008, **62**, 4311–4314.
40 S. Yang, S. Zhu and R. J. C. Hong, *Coatings*, 2020, **10**, 1215.
41 S. B. Kondawar, M. D. Deshpande and S. P. Agrawal, *Int. J. Compos. Mater.*, 2012, **2**, 32–36.
42 F. A. Adesanya and O. E. Fayemi, *Int. J. Electrochem. Sci.*, 2023, **18**, 100382.
43 R. Atchudan, A. Pandurangan and J. Joo, *J. Nanosci. Nanotechnol.*, 2015, **15**, 4255–4267.
44 S. Zhu, A. Xie, B. Wei, X. Tao, J. Zhang, W. Peng, C. Liu, L. Gu, C. Xu and S. Luo, *New J. Chem.*, 2020, **44**, 9288–9297.
45 S. M. Ghoreishi, M. Behpour and M. Golestaneh, *Food Chem.*, 2012, **132**, 637–641.
46 E. C. Hagan, W. H. Hansen, O. G. Fitzhugh, P. M. Jenner, W. I. Jones, J. M. Taylor, E. L. Long, A. A. Nelson and J. B. Brouwer, *Food Cosmet. Toxicol.*, 1967, **5**, 141–157.
47 S. J. Mokole and O. E. Fayemi, *Mater. Res. Express*, 2024, **11**, 105008.
48 M. N. Ranku, G. E. Uwaya and O. E. Fayemi, *Molecules*, 2021, **26**, 5357.
49 X. Qiu, L. Lu, J. Leng, Y. Yu, W. Wang, M. Jiang and L. Bai, *Food Chem.*, 2016, **190**, 889–895.
50 W. Zhang, T. Liu, X. Zheng, W. Huang and C. Wan, *Colloids Surf., B*, 2009, **74**, 28–31.

51 J. Wang, B. Yang, H. Wang, P. Yang and Y. Du, *Anal. Chim. Acta*, 2015, **893**, 41–48.
52 L. Magerusan, F. Pogacean, M. Coros, C. Socaci, S. Pruneanu, C. Leostean and I. O. Pana, *Electrochim. Acta*, 2018, **283**, 578–589.
53 T. Gan, J. Sun, W. Meng, L. Song and Y. Zhang, *Food Chem.*, 2013, **141**, 3731–3737.
54 A. T. E. Vilian, S. M. Kang, S. Y. Oh, C. W. Oh, R. Umapathi, Y. S. Huh and Y. K. Han, *Food Chem.*, 2020, **323**, 126848.
55 M. Wang, Q. Sun, Y. Gao, X. Yang and J. Zhao, *Anal. Methods*, 2014, **6**, 8760–8766.
56 M. Hayat, A. Shah, J. Nisar, I. Shah, A. Haleem and M. N. Ashiq, *Catalysts*, 2022, **12**, 306.